Dynamic aerofracture of dense granular packings

Michael Niebling, Renaud Toussaint, Eirik Grude Flekkøy, Knut Jørgen Måløy

Dynamic aerofracture of dense granular packings.

Michael J. Niebling[1,2,3], Renaud Toussaint[2,3], Eirik G. Flekkøy[1] and Knut Jørgen Måløy[1]
[1] *Department of Physics, University of Oslo, P.O. Box 1048, 0316 Oslo, Norway*
[2] *Institut de Physique du Globe de Strasbourg, CNRS and*
[3] *University of Strasbourg, 5 rue Descartes, 67084 Strasbourg Cedex, France*

A transition in hydraulically induced granular displacement patterns is studied by the means of discrete numerical molecular dynamics simulations. During this transition the patterns change from fractures and fingers to finely dispersed bubbles. The dynamics of the displacement patterns are studied in a rectangular Hele-Shaw cell filled with a dense but permeable two-dimensional (2D) granular layer. At one side of the cell the pressure of the compressible interstitial gas is increased. At the opposite side from the inlet only the gas phase can leave the cell and the grains are stopped by a semipermeable boundary. This imposed pressure gradient causes the grains to compact. In the progress we can identify and describe a mechanism which controls the transition of the emerging displacement patterns from fractures and fingers to finely dispersed bubbles as a function of the interstitial gas' properties and the characteristics of the granular phase.

INTRODUCTION

Hydraulic fractures occur when diverse materials break under the stress induced by fluids or gases. Understanding how hydraulic fracturing is initiated and progresses is of fundamental importance whenever safe dams are constructed, super-critical CO_2 stored or sustainable wells drilled. Volcanic dikes and sills arise naturally by hydraulic fracturing processes. Just as we learn to protect ourselves from the unwanted effects of hydraulic fractures it has been proven to be a useful technology to fracture the reservoir rock formations around a well-bore to enhance the recovery of mineral oil and natural gas.

In previous studies [1–4, 6–15] experiments have been conducted in circular and rectangular Hele-Shaw cells filled with small grains. Under air injection in the center of the circular cell, multiple fingers of low particle density emerged from the inlet [1, 2].

For the rectangular cell it was observed that a decompaction front travels first from the outlet to the inlet before few fingers of low particle density grow from the air inlet [3, 4]. Furthermore, in a recent work, the coarsening of such fingers was studied [5]. In [6] loosely compacted grains have been exposed to a pressure gradient. In the progress of these simulations and experiments a spinodal like instability was observed which displays emerging and growing dispersed bubbles of low particle density.

Considering this background various dynamics and structures have been observed and described. However a theory to explain the transition from dynamics which display dispersed bubbles to dynamics that display fractures and finger like patterns has not been presented. In this article we will study and explain the mechanism that controls the transition between this two types of emerging structures during the compaction of a granular layer.

After a number of experiments have been performed in a rectangular cell [16], we chose to perform numerical simulation. Using a discrete numerical molecular dynamic model we have thereby the possibility to systematically and independently vary the viscosity of the interstitial fluid. Effectively this corresponds to changing the size of the system, as we will discuss in the following. This approach allows to study system sizes which experimentally would be extremely complicated and dangerous to achieve. In the following section we will briefly discuss the parameters and the setup used for the numerical model.

SETUP OF THE NUMERICAL MODEL

The setup is illustrated in Fig. 1. Two glass plates are separated by 1 mm. The space in between the glass plates is filled with dense grains. The gas phase injected at the inlet following the increase of pressure is identical to the gas saturating initially the porous packing. The solid volume fraction of the grains is $\rho_s^{(0)} = 0.42$ which is less than the maximum of $\rho_s^{(\max)} = 0.60$ to allow compaction of the grains. The pressure at the inlet is set to a constant value of $P_I = 2.5 \cdot 10^5$ Pa. The outlet is located on the opposite side of the cell. Here, a semi permeable boundary stops the grains from leaving the cell but is open towards the gas phase. Apart from the semi permeable boundary at the outlet all other three boundaries are fully sealed. At the fully sealed boundaries gas or particle exchange is impossible. Around 200 000 grains of 140±10% μm in diameter are simulated. The size distribution of 10% is set to suppress the formation of a triangular grain packing. Initially the particles are inserted into the cell each with a random velocity. Shortly after the friction between particles and the plates and energy dissipation during particles collisions is activated and the particles build up a fixed random packing. At the start of the simulations the

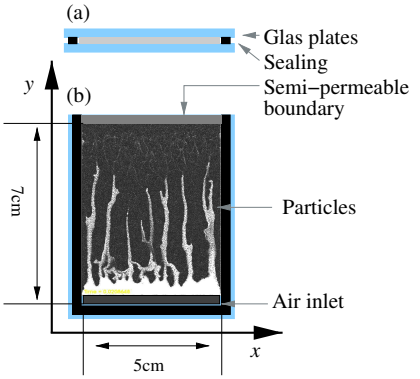

FIG. 1: (Color online) The setup of the system. (a) cross section. (b) top view. Compressed air is injected at the inlet. The outlet is semipermeable: Open towards the gas phase and closed for the granular phase.

pressure at the inlet is increased. Just after the pressure was increased a pressure front starts to propagate through the cell and compacts the particles. The length of the pressure front skin depth is adjusted and varied by changing the gas viscosity.

THEORY AND SIMULATIONS

The numerical model employed is a 2D hybrid model. It uses a continuum description for the gas phase and a discrete description of the granular phase. Friction between particles and the top and bottom plates is included. It was compared to well matched experiments and shown to reproduce closely the dynamics of granular flows at low Reynolds numbers [17–19] and under conditions similar to those assumed in the present article [1].

DYNAMICS OF THE GAS PHASE:

The equations ruling the evolution of the pressure $P = \tilde{P} + P_0$, where P_0 is the atmospheric pressure and $\tilde{P}$ local pressure fluctuations, are derived in detail in Ref. [1, 17, 18, 20–23]. We calculate P according to:

$$\phi\left[\frac{\partial P}{\partial t} + \mathbf{u}\cdot\nabla P\right] = \nabla\cdot\left[P\frac{\kappa}{\mu_f}\nabla P\right] - P\nabla\cdot\mathbf{u}. \qquad (1)$$

This equation basically describes how the divergence of the local granular velocity $\mathbf{u}$ leads to local pressure changes according to the gas displacement by the grains and between them. The viscosity μ_f of the gas determines how fast the gas diffuses through the permeable grains to equalize the pressure fluctuations. $\phi = 1 - \rho_s$ is the local porosity and the local permeability κ is calculated by the Carman-Kozeny relation [20, 25].

DYNAMICS OF THE PARTICLES

The dynamics of each individual particle with the velocity v_p, particle mass $m = \rho_m \pi a^2 h$, particle mass density ρ_m, volume $V_a = \pi a^2 h$ in a cell with a plate spacing of h and the number density defined as $\rho_n = \rho_s \rho_m / m$ is described by:

$$m\frac{dv_p}{dt} = \mathbf{F_I} + \mathbf{F_d} + \mathbf{F_a} - \frac{\nabla P}{\rho_n}. \qquad (2)$$

$\mathbf{F_I}$ are linear inter-particle solid contact forces. The third term on the right hand side of Eq.(2) arises from the momentum exchange between the gas and granular phase. $\mathbf{F_d}$ is a viscous force accounting for energy dissipation during particle collisions. More details are given in [17, 18].
In the granular packing we assume that the normal stress $P_g^{\perp}$ is proportional to the in-plane stress $P_g^{||}$ by a factor λ. This relation is known as the Janssen hypothesis [1, 17]. Considering also a Coulomb friction model we get that the frictional force F_a per particle with the glass plates is proportional to the normal stress by a friction coefficient γ:

$$F_a \leq \gamma S_a(2P_g^{\perp} + \rho_m g h) = \gamma S_a(2\lambda P_g^{||} + \rho_m g h). \qquad (3)$$

The factor 2 in the first term accounts for the two glass plates on each side of the particle. $S_a = \pi a^2$ is the contact area of the particles with the plates. The second term is a contribution due to the gravitational acceleration g on the grains which leads to additional friction between the bottom plate and the particles. This term is included for completeness but has a negligible effect on the following results. Finally, the particle propagation is modeled by the velocity Verlet scheme [26, 27].

RESULTS

The coefficients that determine the friction with the glass plates are set to $\gamma\lambda = 4.0$, a rather high value. Lower values have also been tested and resulted in less branched fractures. The pressure at the inlet is increased as a steep ramp, fast enough that the maximum pressure at the inlet of $P_I = 2.5\cdot 10^5$ Pa is reached before particles significantly start to move. The injected gas is considered as an ideal gas and has the compressibility of air $\beta_T = 1/P_0$. The compressibility is kept constant. The gas viscosity however is increased gradually in different simulations, from the value of air $\mu_f^{(air)} = 0.018$ mPa·s by a factor of 1000 up to $\mu_f = 18.0$ mPa·s. The results

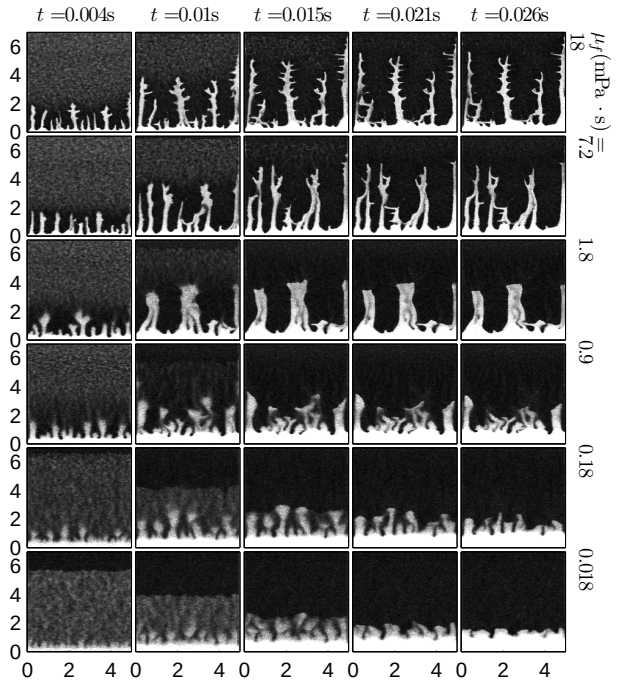

FIG. 2: Snapshots during the simulations of the particle density in the Hele-Shaw cell. Displayed for decreasing gas viscosity from top to bottom and for increasing time (left to right). Low particle density appears brighter in the snapshots. Under air injection, fractures, fingers and dispersed bubbles of low particle density emerge and propagate in time towards the outlet of the cell. x- and y-axis units are given in cm. The y-axis specifies the distance from the inlet. The maximal density is normalized to one.

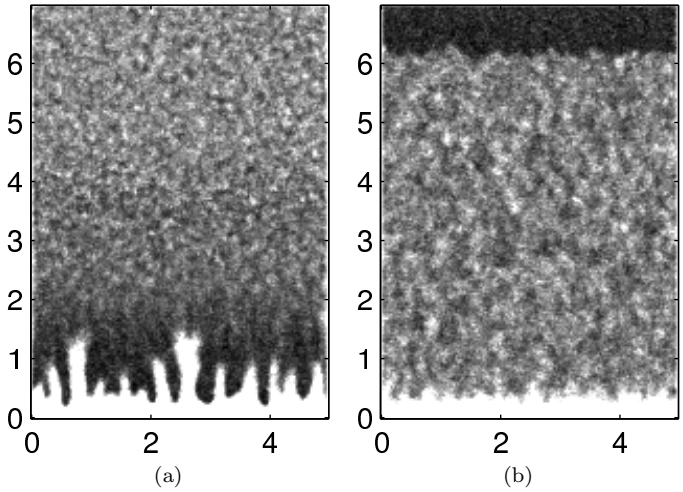

FIG. 3: Zoom in on snapshots of the particle density in the Hele-Shaw cell during the simulations at t =0.003 s. The snapshots correspond to the plots 4(a), 4(d) and 4(g). In (a) $\mu_f = 1.8$ mPa·s and in (b) $\mu_f = 0.018$ mPa·s. The density is normalized to one and the colorbar range is chosen from 0-0.5 to enhance the density contrast. In the plots the darker areas represent higher grain density. In (a) a compaction front at the inlet around the finger tips has emerged. In (b) grains get compacted at the outlet of the cell which corresponds to a darker stripe at the outlet (for y >6 cm).

of the simulations for the particle density are shown in Fig. 2. Dark regions correspond to a high particle density while brighter areas represent low particle density. The gas viscosity decreases from top to bottom while time progresses from left to right. In the time sequences the emerging structures change drastically as a function of the gas viscosity. In the simulation with the lowest gas viscosity dispersed bubbles of reduced particle density appear in the whole cell apart from a darker region at the outlet, where particles get compacted at the semi-permeable boundary (see Fig. 2 for: $\mu_f = (0.18 - 0.018)$ mPa·s; $t = (0.004 - 0.01)$ s or Fig. 3(b) for a zoom in). Increasing the viscosity, structures change from dispersed bubbles to fractures. Furthermore compaction of the grains occurs here at the inlet and in front of the fingers instead of at the outlet. Taking a close look at the simulations at high viscosity in Fig. 2, this is indicated by a dark region in front of the fractures and fingers which were absent for the low viscous cases (see also Fig. 3(a) for a zoom in).

For a better quantification the solid volume fraction is averaged along the x-direction and plotted as a function in the y-direction for three time steps in the Figs. 4(a)-4(c). In these figures compaction of the grains is defined by values of the averaged solid volume fraction higher than 0.45. The inlet side of the cell is just like before located at a y-position close to zero. The outlet is located at $y = 6.9$ cm. At the first time step in Fig. 4(a) we notice that compaction fronts arise at the inlet side for viscosity values of $\mu_f < 0.018$ mPa·s and at the outlet side of the cell for the lowest gas viscosity of $\mu_f = 0.018$ mPa·s. During the next time steps in Figs. 4(b)-4(c) the compaction fronts at the inlet progress towards the outlet. At the outlet compaction of grains now also appears for simulations with gas viscosity values up to $\mu_f = 0.9$ mPa·s. The zone of particle compaction at the outlet grows and expands in time towards the inlet.

To understand how the grain compaction depends on the gas viscosity we will have to take the pressure evolution in the cell into account. In Fig. 5 the gas pressure in the cell is displayed for time steps and gas viscosity values corresponding to Fig. 2. The bottom row, where the gas viscosity has the smallest value in this figure, shows that the pressure decays continuously towards the outlet. Alternatively we can take look at Fig. 4(d) where the pressure average in x-direction is plotted as a function of the y-direction. Confirming our observation from above the Fig. 4(d) shows a linear pressure profile in y-direction for the lowest viscosity right at the start of the simulation. In this regime the pressure gradient acts as a body force displacing all particles in the cell simultaneously and homogeneously and therefore preventing particles from jamming. Furthermore, the homogeneous

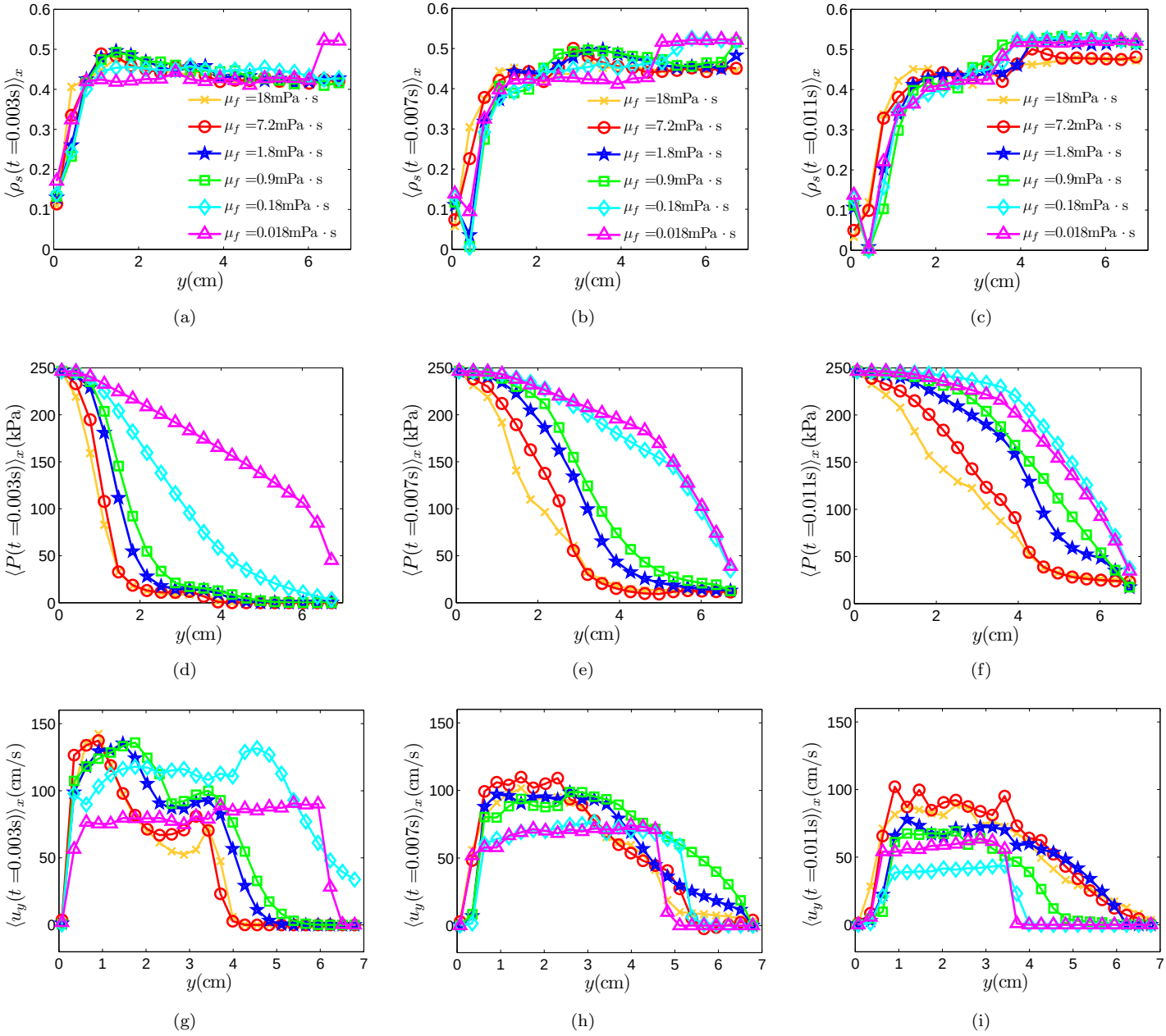

FIG. 4: Several quantities have been averaged along the x-direction and plotted rows from top to bottom: solid volume fraction ρ_s ((a)-(c)), Pressure P ((d)-(f)) and y-component of the grain velocity u_y ((g)-(i)). From left to right the three figures in each row correspond to the times t =0.003, 0.007 and 0.011 s after the start of the injection. Legends are consistent in all plots and only displayed in the first row.

grain motion is also confirmed for the low viscosity value in Fig. 4(g). Here u_y, the y-component of the particle velocity averaged along the x-direction, is constant as a function of y.

The appearance of low particle density bubbles under these conditions has previously been reported and described in [6]. However in the present setup the semi-permeable boundary at the outlet interferes with the otherwise uniform particle motion. This results in the previously mentioned compaction layer at the outlet.

The pressure decay in Fig. 5 becomes more localized if the viscosity is increased. Now the pressure drops rapidly at the interface between the granular phase and the growing particle free region at the inlet side of the cell. Alternatively we can confirm this localized pressure decay in the Figs. 4(d)-4(f) where the pressure is averaged along the x-direction and plotted as a function of y. This time sequence of plots shows that increasing the viscosity re-

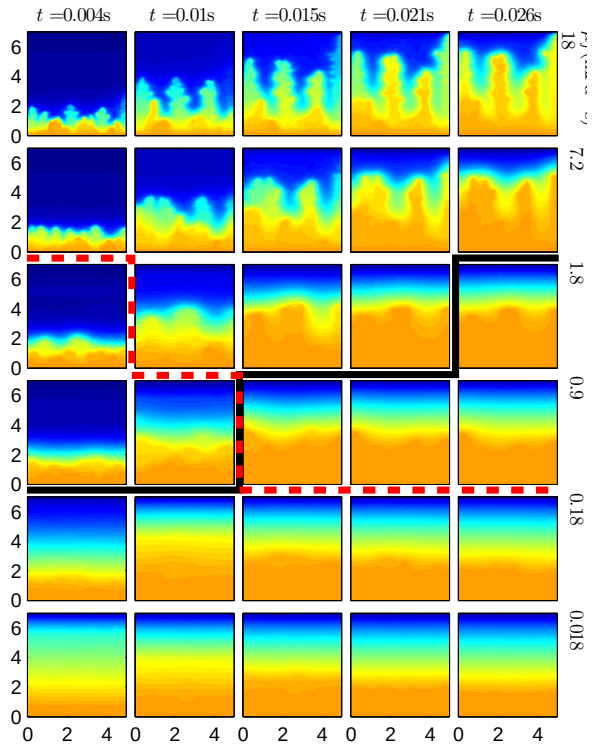

FIG. 5: (Color online) The snapshots show the pressure evolution for decreasing gas viscosity (top to bottom) and as a function of time (left to right). High pressure appears yellow (brighter) in the snapshots. The dashed (red) line between the snapshots shows the time t_f (see Eq.(7). In the snapshots above this dashed (red) line the compaction front thickness is greater then the skin depth of the pressure s defined in Eq. (5). Below the black line, the skin depth s has reached half of the system size in a theoretical system where particles do not move. x- and y-axis units are given in cm. The maximal pressure is normalized to one.

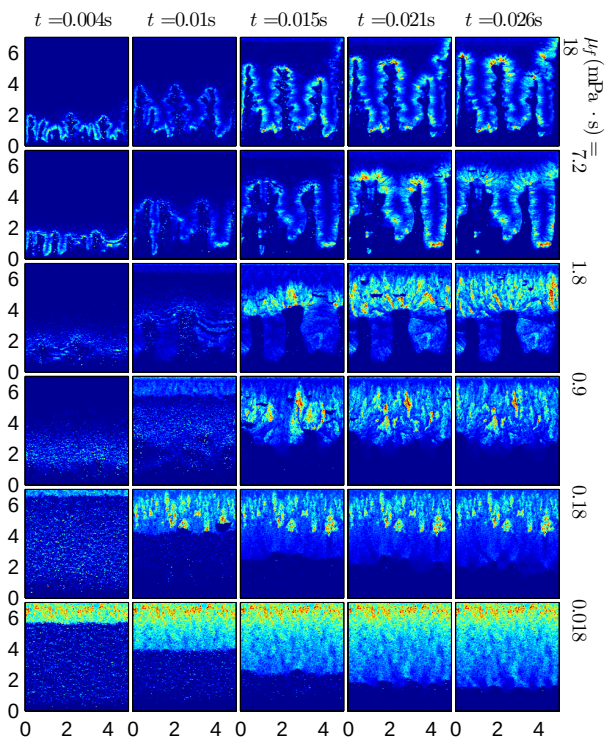

FIG. 6: (Color online) Snapshots of the normal solid in-plane stress between the particles for decreasing gas viscosity (top to bottom) and as a function of time (left to right). High stress appears yellow (brighter) in the snapshots. x- and y-axis units are given in cm. The maximal normal solid in-plane stress is normalized to one.

sults in an increasingly steep pressure decay at the interface. Further inside the granular packing towards the outlet the pressure remains initially unchanged. In this regime the pressure gradient acts as a surface force on the particles at the interface between granular and gas phase. Due to the localized pressure gradient particles at the interface close to the pressure inlet are initially stronger accelerated than the particles close to the outlet. This leads to particle collisions and jamming in the granular packing at the interface where a compaction front builds up.

Where the grains are compacted the solid stress increases as displayed in Fig. 6. The solid stress is shown to increases first at the outlet for the least viscous gas. For higher viscosity values the solid stress is localized around the finger tips. Here the solid stress decays inside the granular packing over a certain distance which is of the size as the compaction front. This distance can be larger than the distance over which the pressure gradient decays from the interface into the granular packing. In this regime the particles further inside the packing are accelerated through solid contacts rather than by the pressure gradient of the fluid. Such solid contacts in a compacted granular medium transmit the stress localized along distinct force chains. This causes a heterogeneous acceleration of the particles and the particle velocity in y-direction is increased along certain localized paths, as shown in Fig. 7. Local noise and disturbance are now affecting the evolution of the interface directly and fractures appear.

In this situation local particle rearrangement and jamming results in the observed fracture pattern. To quantify the transition between the two regimes we will briefly define the characteristics of the pressure diffusion, as done in detail in [18]. We neglect the motion of the granular phase and consider a standard diffusion equation for the pressure evolution within the granular phase. This approach allows to define a diffusion constant for the pressure

$$D = \frac{\kappa}{(1-\rho_s)\beta_T \mu_f}. \tag{4}$$

Furthermore we define a skin depth

$$s = \sqrt{4Dt}. \tag{5}$$

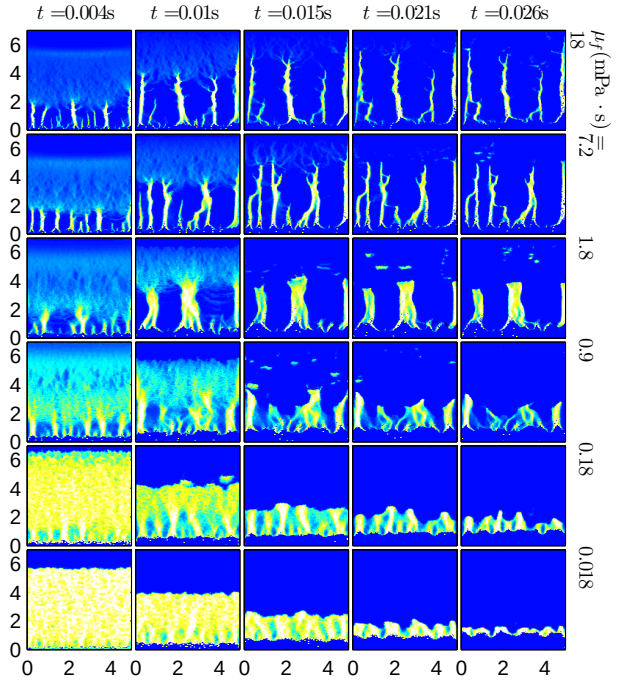

FIG. 7: (Color online) Snapshots of u_y, the y-component of the particle velocity for decreasing gas viscosity (top to bottom) and as a function of time (left to right). High velocity appears yellow (brighter) in the snapshots. x- and y-axis units are given in cm. u_y is normalized to one.

s is the distance from the gas/particle interface over which the pressure has decayed by $P(s) = \frac{1}{e}P_I$ [28]. The diffusion constant in Eq. (4) specifies how fast the fluid flow can equalize pressure changes at given gas properties and characteristics of the porous medium.

We can compare how well this assumed pressure evolution fits to the simulations. For this purpose we average the pressure in x-direction and calculate the maximum gradient in y-direction of this pressure average: $\max(\partial_y \langle P \rangle_x)$ as a function in time (see Fig. 8(b) for all viscosity values). The y-position of $\max(\partial_y \langle P \rangle_x)$ propagates from the inlet towards the outlet as time passes as shown in Fig. 8(a). At low viscosity the position of the maximum gradient reaches the outlet almost immediately after the simulation has started while at high viscosity values this maximum gradient never reaches the outlet during the simulated time.

In Fig. 8(a) the y-position of $\max(\partial_y \langle P \rangle_x)$ depends on the combined position of the skin depth and the position of the gas/particle interface. To study the pressure evolution relative to the gas/particle interface at the finger tip in a Lagrangian reference frame it is more useful to calculate $\max(\partial_y \langle P \rangle_x)$ as a function in time. If the assumed propagation of the skin depth for the pressure as a square root in time relative to the interface is correct we should be able to rescale $\max(\partial_y \langle P \rangle_x)$ by multiplication with the skin depth $s(t)$ defined in Eq. (5). The rescaling is done in Fig. 8(c). The rescaled graphs are constant in time. This supports the proposed diffusive pressure behavior relative to the particle motion. For low viscosity values the rescaling does not result in a constant behavior because of the limiting finite size of the cell. Further more we observe that the plots do not fall directly above each other. For increasing viscosity values the graphs are shifted downwards by a constant. This effect is not captured in our explanation and is most likely due to rearrangements and motion of the particles. In the following the skin depth is used as a measure of how steep and how far the pressure decays into the granular phase in the cell.

We notice in Eq. (4 and 5) that increasing the viscosity reduces the skin depth. Using Eq. (5) the calculated time for the skin depth to propagate through the cell in y-direction is 0.0009 s at the lowest viscosity value. This is faster than the time needed to notice a significant movement of the grains. For the highest viscosity value in the simulations the calculated time is 0.9 s until the skin depth has grown to the size of the cell assuming a fixed granular packing.

At the very start of the simulations the evolution of the system is controlled by two length scales. The first length scale is the length of the skin depth. The second length scale is the thickness of the compaction front at the gas/particle interface at the inlet. Before fractures appear the thickness of this compaction front is related to the growth of the particle free zone at the inlet. When the particle free zone at the inlet of the cell grows to a certain length of Y_t in y-direction from the inlet the displacement of the particles leads to a compaction front with a minimal thickness of

$$d_c = \frac{Y_t \rho_s^{(0)}}{\rho_s^{\max} - \rho_s^{(0)}}. \tag{6}$$

Where d_c depends on the initial solid volume $\rho_s^{(0)}$ fraction and the possible maximal volume fraction $\rho_s^{\max}$ of the grains. Before fractures appear Y_t is equivalent to the position of the most advanced finger tip which is plotted in Fig. 9. The figure shows that the particle free zone at the inlet progresses linearly in time for all viscosity values with constant velocity $\dot{Y}_t$ until complete particle compaction occurs at $t > 0.01$s. For the viscosity value of $\mu_f = (0.18)$ mPa·s distinct fingers and fractures are yet not formed. Nevertheless, the figure shows that the growing particle free zone at the pressure inlet already progresses linearly in time before fingers form. According to Eq. (6) this also implies a linear growth in time for the thickness of the compaction front. However, the pressure skin depth increases proportionally to the square root in time as shown in Eq. (5). At a certain transition time

$$t_f = \frac{4D}{\dot{d}_c^2} \tag{7}$$

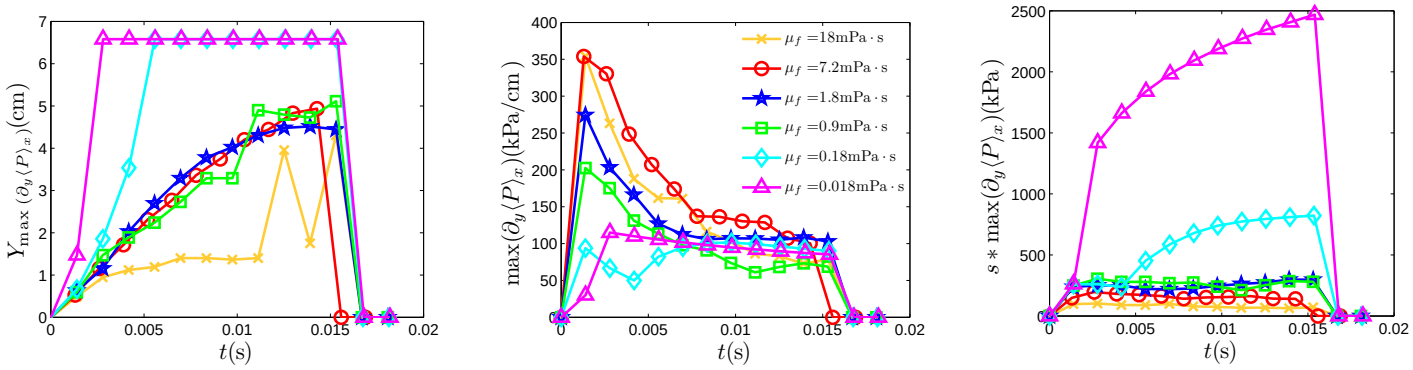

FIG. 8: (a) shows the y-position of the maximum gradient in y-direction of the in x-direction averaged pressure $\langle P\rangle_x$ as a function in time. Fig. (b) shows the maximum value of the pressure gradient in y-direction of $\partial_y\langle P\rangle_x$ the in x-direction averaged pressure. In Fig. (c) this maximum derivative is rescaled by the skin depth $s = \sqrt{4Dt}$. Legends are consistent in all plots and only displayed in the middle figure.

the thickness of the compaction front d_c will therefore overtake the skin depth s.

At time t_f we expect the transition from a body force to a surface force and the appearance of fractures instead of dispersed bubbles. For a direct comparison we visualized the transition time t_f in Fig. 5 by a dashed (red) line. Above this line the thickness of the compaction front is larger than the skin depth. When the compaction front is ahead of the skin depth fractures were predicted in the previous discussion. The fractures in the Figs. 2 and 5 emerge at the predicted time and thus demonstrate a good agreement between the analytical prediction and the simulations.

After fingers emerge in the regime of high gas viscosity ($\mu_f > 0.9$ mPa·s) the compaction front propagates at a constant speed through the cell. This is shown in Fig. 10(a) where the y-position of the maximum solid volume fraction averaged in x-direction $\max(\langle\rho_s\rangle_x)$ is plotted in time.

In Fig. 10(b) we plotted the thickness of the particle compaction front in time. Although the data is very noisy it can be seen that the thickness of the compaction front for all tested viscosity values initially grows in time. The compaction front for a gas viscosity $\mu_f < 0.9$ mPa·s is located at the outlet of the cell and the thickness grows until complete compaction of the grains. The more interesting values are found for a gas viscosity of $\mu_f > 1.8$ mPa·s. Because here the compaction front is located at the gas/particle interface and the thickness is measured during the fracturing of the granular packing takes place. In this regime for the two highest viscosity values an initial increase of the compaction front thickness occurs. After a time of approximately $t = 0.002$s the growth of the compaction front thickness slows down and appears to stay rather constant during the further propagation

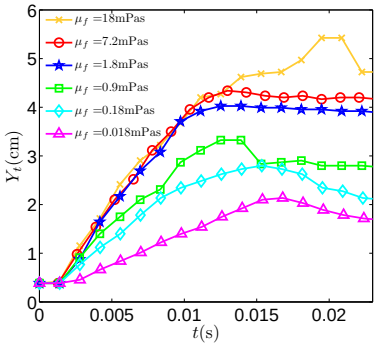

FIG. 9: (Color online) The position of the most advanced finger tip Y_t as a function in time and for different viscosity values. The position of the most advanced finger was found by normalizing the particle density by its maximum value and averaging in x-direction. If this averaged particle density drops to a value of 0.85, approaching from the outlet side of the cell, we define the corresponding y-position: Y_t as the position of the most advanced finger tip.

of the fractures until boundary effects start to play a role and the grains get completely compacted. This happens at $t \approx 0.01$s for the gas of highest viscosity and at $t \approx 0.007$s for the gas with viscosity of $\mu_f = 1.8$ mPa·s.

Reducing the skin depth by increasing the viscosity has the same effect on the pressure evolution as increasing the system size instead. We can demonstrate this in the following discussion by non-dimensionalize Eq.(1). We have previously shown that when the gas viscosity is increased the pressure drop gets more and more localized along the interface between the gas and the grains. Thus continuously a limit is approached where only the outermost particles at the interface are accelerated by the pressure

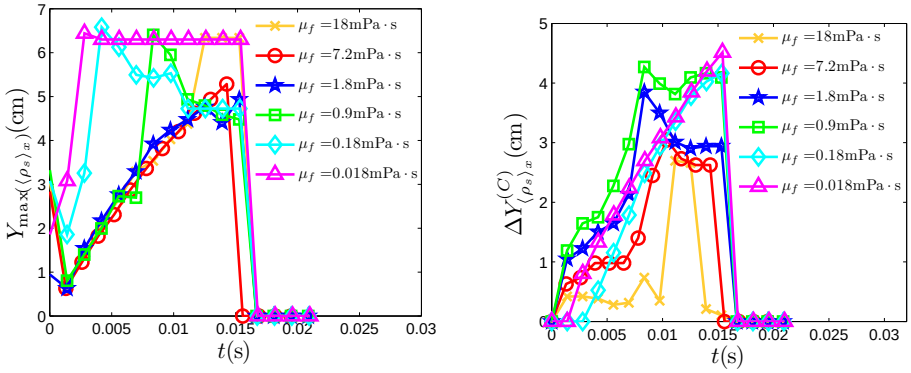

(a) (b)

FIG. 10: In (a) the y-position of the maximum solid volume fraction $\max(\langle\rho_s\rangle_x)$ in time is plotted. Before the position of the maximum is calculated the solid volume fraction is the cell was averaged along the x-direction. In (b) $\Delta Y^C_{\langle\rho_s\rangle_x}$ a measure of the compaction front thickness is plotted. It is the distance in y-direction over which the $\langle\rho_s\rangle_x$ value lies above a threshold of 0.47 as a function in time.

gradient. The presented simulations approach this limit of a pure surface force. As a consequence the velocity of the finger tip in Fig. 9 reaches a maximal value for a gas viscosity above $\mu_f = (0.9)$ mPa·s. This maximal characteristic velocity for the finger tips in the plots is measured to be around $U_0 = 470$ cm/s and stays constant for $t < 0.01$ s. Further increase of the gas viscosity will not significantly increase the maximal velocity of the finger tips. In the limit of a pure surface force this maximal velocity is now primarily dependent on the injection pressure and on the properties of the granular phase.
To non-dimensionalize Eq.(1) we use this characteristic velocity U_0 to define a dimensionless velocity $u = U_0 u'$ and introduce $\kappa_0 = a^2/9K$ as the characteristic magnitude of the permeability. To define further dimensionless variables we use the system size l as a characteristic length scale with $x = lx'$ and $y = ly'$. The atmospheric pressure P_0 is used as a the characteristic pressure to define $P = P_0 P'$. From these quantities follows a characteristic time scale $\tau = l/U_0$ and $t = \tau t'$ [20]. The resulting non-dimensionalized equation is:

$$\phi\left[\frac{\partial P'}{\partial t'} + \mathbf{u}'\cdot\nabla' P'\right] = \frac{1}{\mathrm{Pe}}\nabla'\cdot\left[P'\frac{(1-\rho_s)^3}{\rho_s^2}\nabla' P'\right] - P'\nabla'\cdot\mathbf{u}'. \tag{8}$$

In this equation the Peclet number was defined as

$$\mathrm{Pe} = \frac{U_0\mu_f l}{P_0\kappa_0}. \tag{9}$$

This analysis shows that alternatively changing the viscosity, the length scale or the inverse permeability has the same effect on Eq. 8 that describes the pressure evolution. Increasing the gas viscosity is equivalent as using a larger system or reducing the permeability.

CONCLUSION:

The emerging structures sensitively depend on whether the particles are accelerated primarily by solid contacts or by the imposed pressure gradient. We could show that the evolving structures depend on a characteristic length scale which is given by the skin depth s. For a skin depth larger than the system size, large scale homogeneous motion and the formations of dispersed bubbles are the results. For a short skin depth compared to the system size a compaction front builds up that allows fracturing. Hence, controlling the time dependence of the injection pressure should in principle allow one to control the pressure response in the packing, and transit from fracturing to diffusely compacting regimes. It should also in principle enable to fracture a porous rock at adjustable distances from the inlet.

[1] Ø. Johnsen, R. Toussaint, K. J. Måløy, and E. G. Flekkøy, Phys. Rev. E **74** 011301 (2006).
[2] X. Cheng, L. Xu, A. Patterson, H. M. Jaeger, S. R. Nagel, Nat Phys, **4**, 234-237 (2008).
[3] Ø. Johnsen, C. Chevalier, A. Lindner, R. Toussaint, E. Clément, K.J. Måløy, E.G. Flekkøy and J. Schmittbuhl, Phys. Rev. E **78**, 051302 (2008).
[4] Ø. Johnsen, R. Toussaint, K.J. Måløy, E.G. Flekkøy and J. Schmittbuhl, Phys. Rev. E **77**, 011301 (2008).
[5] M. J. Niebling, R. Toussaint, E. G. Flekkøy and, K. J. Måløy, Rev. Cub. Fis. 29, 1E66 (2012).
[6] J. L. Vinningland, E. G. Flekkøy, K. J. Måløy and R. Toussaint (unpublished)
[7] A. Nermoen, C. Raufaste, S. D. de Villiers, E. Jettestuen, P. Meakin, D. K. Dysthe. Physical Review E **81**, 061305, (2010).
[8] S. D. de Villiers, A. Nermoen, B.Jamtveit, J. Mathiesen,

P. Meakin, S.C. Werner, (unpublished)
[9] M.A. van der Hoef, M. van Sint Annaland, and J.A.M. Kuipers, Chem. Eng. Sci. **59**, 5157 (2004).
[10] N.G. Deen, M. van Sint Annaland, M.A. van der Hoef, and J.A.M. Kuipers, Chem. Eng. Sci. 62, 28 (2007).
[11] N.G. Deen, M. van Sint Annaland, M.A. van der Hoef, and J.A.M. Kuipers, Progress in Computational Fluid Dynamics 7, 152 (2007).
[12] M.A. van der Hoef, M. van Sint Annaland, N.G. Deen, and J.A.M. Kuipers, Ann. Rev. Fluid Mech. 40, 47 (2008).
[13] C. Zeilstra, J.G. Collignon, M.A. van der Hoef and J.A.M. Kuipers, Powder Tech. 184, 166 (2008).
[14] B. Sandnes, E.G. Flekkøy, H.A. Knudsen, K.J. Måløy, H. See, Nature Communications 2, 288 doi:10.1038/ncomms1289 (2011).
[15] T. Börzsönyi, R.E. Ecke and J.N. McElwaine, Phys. Rev. Lett. 103, 178302 (2009).
[16] M. Schelstraete, J. Schmittbuhl, R. Toussaint, Master thesis, University of Strasbourg, France, (2008-2009).
[17] M. J. Niebling, E. G. Flekkøy, K. J. Måløy and R. Toussaint, Phys. Rev. E **82** 011301 (2010).
[18] M. J. Niebling, E. G. Flekkøy, K. J. Måløy and R. Toussaint, Phys. Rev. E **82** 051302 doi: 10.1103/PhysRevE.82.051302 (2010).
[19] J. L. Vinningland, R. Toussaint, M. Niebling, E. G. Flekkøy, and K. J. Måløy, Europhys. Lett. **204**, 27-40, Number 1 (2012) doi: 10.1140/epjst/e2012-01550-2.
[20] S. McNamara, E.G. Flekkøy and K.J. Måløy, Phys. Rev. E **61** 4054 (2000).
[21] J. L. Vinningland, Ø. Johnsen, E. G. Flekkøy, R. Toussaint and K. J. Måløy, Phys. Rev. Lett. **99** 048001 (2007).
[22] J. L. Vinningland, Ø. Johnsen, E. G. Flekkøy, R. Toussaint and K. J. Måløy, Phys. Rev. E **76** 051306 (2007).
[23] J. L. Vinningland, E. G. Flekkøy, R. Toussaint and K. J. Måløy, Phys. Rev. E **81**, 041308 (2010).
[24] D.-V. Anghel, M. Strauss, S. McNamara, E.G. Flekkøy and K.J. Måløy, Phys. Rev. E **74** 029906(E) (2006)
[25] P.C. Carman, Trans. Inst. Chem. Eng. **15**, 150 (1937).
[26] E. G. Flekkøy, R. Delgado-Buscalioni and P. V. Coveney, Phys. Rev. E **72** 026703 (2005).
[27] W. H. Press, W.T. Vetterling "Numerical Recipes", Cambridge University Press (2002).
[28] E. Butkov "Mathematical Physics", Addison Wesley (1968).